

The selective reductive amination of aliphatic aldehydes and cycloaliphatic ketones with tetragonal zirconium dioxide as the heterogeneous catalyst



Shun Wang, Jiacong Li, Ming Zhang*, Peng Bai, Haigang Zhang, Xinli Tong*

Tianjin Key Laboratory of Organic Solar Cells and Photochemical Conversion, Tianjin Key Laboratory of Drug Targeting and Bioimaging, School of Chemistry and Chemical Engineering, Tianjin University of Technology, No. 391 Binshuixi Road, Tianjin, 300384, China

ARTICLE INFO

Keywords:

Reductive amination
Catalysis
Aliphatic aldehydes
Ketones
Zirconium oxide
DFT calculations

ABSTRACT

A selective reductive amination of aliphatic aldehydes and cycloaliphatic ketones is achieved with *tetragonal* zirconium dioxide (*t*-ZrO₂) as the catalyst. With *N,N*-dimethyl formamide (DMF) as the solvent, low-molecular-weight amine source and reductant, a more than 99 % yield of *N,N*-dimethylpentan-1-amine or *N,N*-dimethyl cyclohexanamine was obtained when *n*-pentanal or cyclohexanone was used as the substrate. Particularly, the crystallographic structures exhibit a significant effect on catalytic performance where the *tetragonal* crystalline was preferable to *monoclinic* one during the reductive amination reaction. In addition, the recycling experiments of catalysts indicate that *t*-ZrO₂ still kept a high catalytic activity even after being reused five times. From the result of DFT calculations, it is concluded that the crystalline of zirconium dioxide is closely related to the charge transferring rate between the catalyst and the adsorbed reactant. Finally, based on the experiment phenomena and simulation result, a possible reaction mechanism is proposed for the reductive amination of cyclohexanone.

1. Introduction

N-alkylamines are often used as versatile building blocks for the production of agrochemicals, fine chemicals and pharmaceuticals in organic or biological system [1–4]. Therefore, a series of methods that enable efficient synthesis of *N*-alkylamine have been pursued intensively. Among these different techniques available, the most well-established and facile approach to synthesize *N*-alkylamines should be direct reductive amination of carbonyl compound [5–8]. Therein, aldehydes or ketones are chosen as feedstocks to afford the desired products by reacting with amines in the presence of reductant such as borohydrides or H₂.

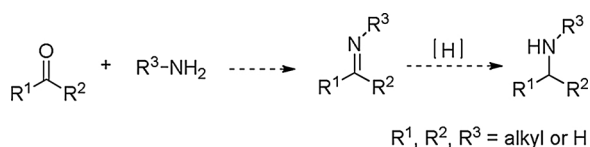
As shown in **Scheme 1**, the classic process of reductive amination of carbonyl compounds involves two steps where the C=N double bond could be generated from the condensation process and then the hydrogenation of the corresponding imine derivatives would be further performed [9,10]. Therein, the synthesis of *N,N*-dimethyl tertiary amines often employ the aldehydes and dimethyl amines to react *via* the homogeneous transition metal-catalyzed hydrogenation using stoichiometric borohydrides as reductants [11–14]. However, the use of a stoichiometric amount of boron hydrides causes the generation of numerous wastes, the decrease of selectivity of target product and the toxicity matter. When the H₂ was used, the catalytic hydrogenation process generally demands noble metal catalyst and expensive ligand in

homogeneous catalytic system [15–17], sometimes with low atomic efficiency [18,19], and the difficult separation of metal catalyst and product; especially, the catalyst recycling is always a troublesome question; besides, the manipulation of hydrogen is dangerous for laboratory or industrial production. In view of the demand for green chemistry, there are a lot of places and routes for improvement.

Very recently, the synthesis of *N*-alkylamine to generate a single product in one step by a more sustainable synthesis route is presented, in which a homogeneous Zn(OAc)₂-catalyzed reductive amination of aldehydes and ketones with *N,N*-dimethyl formamide (DMF) is achieved *via* the *in situ* generated Me₂NH and HCOOH that can be used to synthesize the *N,N*-dimethyl tertiary amine in a simple process [20]. While, the separation and reuse of catalyst is still not resolved now. Therefore, the process of synthesizing *N,N*-dimethyl tertiary amines in one-step *via* heterogeneous catalysts is a promising orientation. In previous communication, we investigated the promotion of different metal oxides on the reductive amination of aromatic aldehydes and found that zirconium oxide as heterogeneous catalyst was superior to other metal oxides [21]. However, little research on the reductive amination of ketones and aliphatic aldehydes were carried out; particularly, the mechanism on heterogeneous catalytic reduction amination keeps unclear at present. Herein, the catalytic performances and mechanism of zirconium oxide on the transformation of aliphatic aldehydes and ketones will be studied in detail.

* Corresponding authors.

E-mail addresses: 13820981259@163.com (M. Zhang), tongxinli@tju.edu.cn, tongxli@sohu.com (X. Tong).



Scheme 1. The reductive amination of carbonyl compounds.

It is well-known that there are three crystal forms of ZrO_2 including the cubic, tetragonal and monoclinic crystals. The monoclinic phase keeps stable at room temperature, and is transformed to tetragonal one at 1170 °C, and then transformed to cubic one at 2370 °C [22]. In these forms, the metastable tetragonal one (*t-ZrO₂*) exhibits particular interest which probably exhibits preferable catalytic and mechanical property compared to the cubic one (*c-ZrO₂*) and monoclinic one (*m-ZrO₂*) [23]. In order to realize the synthesis of zirconia nanoparticles, several efficient methods have been investigated which include the sol-gel process [24], spray pyrolysis [25], magnetron sputtering [26], hydrothermal methods [27], carbon nanotube templated method [28], and emulsion precipitation [29].

In this article, the *m-ZrO₂*, *t-ZrO₂* and other oxides are prepared by simple precipitation method, and employed as the heterogeneous catalysts for the reductive amination of different ketones and aliphatic aldehydes. As a result, the *t-ZrO₂* showed the highest catalytic activity and provided the satisfactory yields of the target products. Based on the DFT calculation and characterization results of catalysts using XRD, BET, SEM, TEM, NH_3 -TPD, FT-IR, Pyridine-IR and TGA techniques, the relationship between the structures and catalytic performances are discussed.

2. Experimental section

2.1. Reagents and experimental equipment

The reagents are of analytical grade and were purchased from commercial vendors, which include *N, N*-dimethylformamide (DMF), $ZrCl_4$, $ZrOCl_2$, NaOH, TiO_2 , Al_2O_3 , CeO_2 , MgO, ZnO, KBr and formic acid, pyridine, 2,2'-dipyridine, dimethylamine, cyclohexanone, cyclobutanone, cyclopentanone, cycloheptanone, cyclooctanone, butaldehyde, caproaldehyde, valeraldehyde, heptaldehyde, 2-heptanone, 2-pentanone, 3-pentanone. The nitrogen stored in the high-pressure cylinder is used directly through the pressure reducing valve without further treatment.

X-ray powder diffraction (XRD) patterns were obtained using a Rigaku/Max 2500/PC powder diffractometer with Cu K α radiation at a scan range (2θ) of 5–80°. The surface morphology observation was performed on scanning electron microscope (SEM: JSM-6301 F, JEOL) and the interior morphology was characterized by transmission electron microscope (TEM: JEM-2100, JEOL). The Brunauer-Emmett-Teller (BET) surface area of the sample were measured by N_2 adsorption using an ASAP2020 M system. All the sample were degassed at 200 °C under vacuum before N_2 adsorption measurements. Fourier transform infrared (FT-IR) and Pyridine infrared (Py-IR) spectra were obtained on a Bruker Tensor 27 spectrometer with dried KBr or pyridine, respectively. Thermogravimetric (TG) was performed by NETZSCH-TG209 F3, heating in N_2 at 10 °C min⁻¹ rate. NH_3 -TPD was performed on a Micromeritics' ChemiSorb 2720 TPx system.

The analysis of liquid products was performed by gas chromatography-mass spectrometry (Agilent 7890A/5975C). The nuclear magnetic resonance (NMR) measurement was achieved by a Bruker 400 MHz spectrometer. The conversion and selectivity were determined using an internal standard method and area normalization method, respectively.

2.2. Synthesis of ZrO_2 with different calcination temperature

Typically, 40 mL $ZrCl_4$ aqueous solution (0.16 mol/L) was placed in a beaker, and its pH was adjusted to 10 via dropwise addition of 0.1 mol/L NaOH aqueous solution with vigorous stirring and monitored with a pH meter. After 72 h of aging, the suspension was filtered, washed with deionized water to pH = 7, and then the obtained solid was dried under vacuum at 80 °C for 12 h. After milling, a $Zr(OH)_4$ catalyst was obtained. Then, the $Zr(OH)_4$ powder was calcined respectively at 400, 500, 600, 700, 800 and 900 °C to obtain ZrO_2 -400, ZrO_2 -500, ZrO_2 -600, ZrO_2 -700, ZrO_2 -800, and ZrO_2 -900. The ZrO_2 with the 500 °C and ZrO_2 with 900 °C were named as *t-ZrO₂* and *m-ZrO₂* respectively.

2.3. General procedure for reductive amination of ketones and aliphatic aldehydes

All the reductive amination experiments are performed in a 120 mL autoclave equipped with the magnetic stirring and automatic temperature control. A typical procedure for reductive amination of cyclohexanone is given as follows: the substrate cyclohexanone (0.20 g), *t-ZrO₂* (0.050 g), H_2O (0.500 g) and *N, N*-dimethylformamide (15 mL) were charged into the reactor, and the atmosphere inside was replaced by the pure nitrogen after the reactor is sealed. Under stirring, the nitrogen is charged to 0.3 MPa at room temperature, and the autoclave was heated to 140 °C and was kept for 4 h. After reaction, the autoclave is slowly cooled to room temperature and the solid catalyst is separated by ultrafiltration membrane. The mixture is analyzed by an Agilent 7890A/5975C GC equipped with an HP-5MS column and FID detector.

2.4. Density functional calculations

Calculations were carried out in the framework of density functional theory (DFT) by using CASTEP module in the Materials Studio of Accelrys, Inc. The nonlocal exchange and correlation energies were calculated with the Perdew-Wang (PW91) functional of the generalized gradient approximation (GGA) [30,31]. A plane-wave basis set with a cutoff energy of 400 eV was used to expand the valence electrons. The geometries were optimized using a BFGS method [32] with spin polarization. The convergence criteria included threshold values of 2×10^{-5} eV/atom, 0.05 eV/Å and 0.002 Å for energy, maximum force and maximum displacement, respectively, and the self-consistent-field (SCF) density convergence threshold value of 2.0×10^{-6} eV/atom.

On basis of the experimental evidence (XRD results in Fig. 1), the (-1 1 1) surface of monoclinic zirconia (*m-ZrO₂*) and (0 1 1) surface of tetragonal zirconia (*t-ZrO₂*) were employed in the DFT calculations in this research. The 2×2 (*m-ZrO₂*) and 3×2 (*t-ZrO₂*) surface supercells were used for surface slabs, respectively; the corresponding formulas are $Zr_{44}O_{76}$ and $Zr_{36}O_{60}$. The bottom 3 layers were fixed to that of the corresponding polarization bulk structures, while the top 8 layers for *m-ZrO₂* (-1 1 1) and 5 layers for *t-ZrO₂* (0 1 1) were relaxed respectively. The vacuum region thickness between slabs was 20 Å, which was large enough to avoid the inter-planar interaction generated by periodic boundary conditions. The surface Brillouin zone was sampled by a $2 \times 2 \times 1$ Monkhorst-Pack grid [33]. All the adsorption molecules were fully relaxed. The structures of *m-ZrO₂* (-1 1 1) and *t-ZrO₂* (0 1 1) surface were given in Figure S11 of the Supporting Information.

In order to describe the interaction between adsorption molecules and ZrO_2 surface, the adsorption energy (E_{ads}) was defined as following [34,35]:

$$E_{ads} = (E_{DMF/ZrO_2} - E_{DMF} - E_{ZrO_2})$$

where E_{DMF/ZrO_2} was the total energy of the ZrO_2 slab with adsorbed DMF, E_{DMF} was the energy of isolated DMF molecule in gas phase, E_{ZrO_2} was the energy of a clean ZrO_2 slab.

The $E_{C-N/gas}$ and E_{C-N/ZrO_2} were used to describe the C–N bond strength of DMF molecular in gas and adsorbed on the ZrO_2 surface,

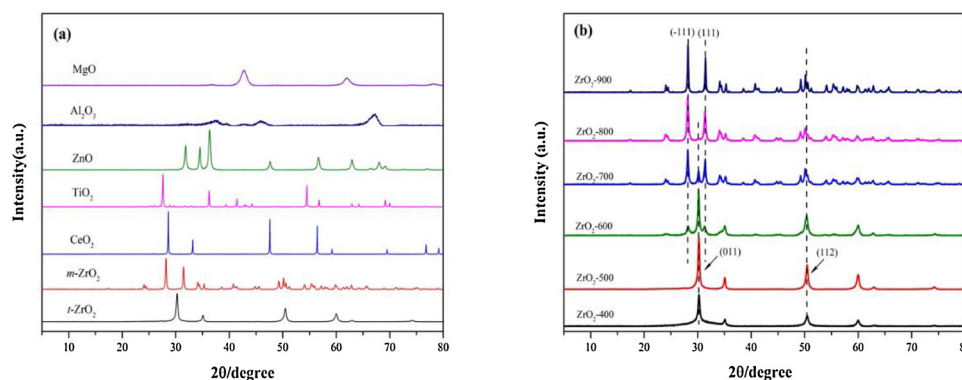


Fig. 1. XRD patterns of (a) different metal oxides and (b) ZrO₂ with different calcination temperatures.

respectively. The calculated formulas were defined as following:

$$E_{C-N/gas} = -(E_{DMF} - E_{DMF(broken)})$$

$$E_{C-N/ZrO_2} = -(E_{DMF/ZrO_2} - E_{DMF(broken)/ZrO_2})$$

Where E_{DMF} was the energy of the isolated DMF molecule in gas phase, $E_{DMF(broken)}$ was the total energy of two segments ($-N(CH_3)_2$ and $-COH$) obtained by broken C–N bond of DMF in gas phase; E_{DMF/ZrO_2} was the total energy of the ZrO₂ slab with adsorbed DMF, $E_{DMF(broken)/ZrO_2}$ was the total energy of ZrO₂ slab with two segments ($-N(CH_3)_2$ and $-COH$).

2.5. The calculation formulas for substrate conversion and product selectivity

Conv. (%)

$$= \frac{\text{The total amount of substrates} - \text{the leftover amount of substrates}}{\text{The total amount of substrates}} \times 100\%$$

$$\text{Yield}(\%) = \frac{n_p}{n_s} \times 100\%$$

$$\text{Sel.}(\%) = \frac{\text{Yield}(\%)}{\text{Conv.}(\%)} \times 100\%$$

The conversion of substrate was obtained by the internal standard method (1,3-dichlorobenzene as the internal standard) and standard curve of substrate (Fig. S5). The yield and selectivity of product was obtained by the standard curve of product (Fig. S5). Where n_p is the mol of product, n_s is the mol of substrate.

3. Results and discussion

3.1. The characterization of catalysts

The crystalline structures of the used metal oxides were investigated by means of XRD and the patterns were shown in Fig. 1. See from the obtained results, it is confirmed that the crystal of metal oxides is successfully prepared where the diffraction peaks are quite sharp and regular (Fig. 1a). Moreover, the *t*-ZrO₂ is successfully prepared by calcination at 500 °C and *m*-ZrO₂ is synthesized by calcination at 900 °C, respectively. Fig. 1b indicates the characteristic peaks situated at $2\theta = 30.27^\circ$ and 50.37° correspond to the (011) and (112) reflection planes, respectively, which match with the tetragonal phase of ZrO₂ material well. The diffraction peaks situated at $2\theta = 28.17^\circ$ and 31.46° correspond to the (-111) and (111) reflection planes, which match with the monoclinic phase of ZrO₂ material well. Also, it is found the crystallinity of these two crystal forms is relatively high according to results of XRD patterns. Moreover, the transition from tetragonal to monoclinic

can be seen clearly from the Fig. 1; therein, when the temperature is 500 °C, the crystallinity of tetragonal ZrO₂ is relatively high; as the temperature increases, the content of monoclinic ZrO₂ increases continuously. When it rises to 900 °C, the crystal forms no longer change, and it becomes completely monoclinic ZrO₂. Obviously, a higher temperature facilitates monoclinic zirconia formation, and an increasing intensity of these peaks was observed with the increase of the calcination temperature.

The morphologies and microstructures of catalysts were examined by SEM and TEM instruments and the results are presented in Fig. 2. As a result, it can be seen that *t*-ZrO₂ was a sheet structure and *m*-ZrO₂ was a spherical structure. Generally, the flake catalysts have a larger specific surface area than the spherical ones. In addition, it is found that, from the TEM images, the size of *t*-ZrO₂ is smaller than that of *m*-ZrO₂, which may be attributed to the occurrence of particle aggregation. In addition, it can be found that ZrO₂-500PA was still tetragonal ZrO₂, but the crystallinity is relatively low compared to that of ZrO₂-500 catalyst (seen from Fig. S4). Furthermore, the average particle size of *t*-ZrO₂ and *m*-ZrO₂ catalyst was respectively 153 nm and 242 nm by using the Scherrer's equation, which keeps almost consistent with the obtained results from the TEM images.

In order to further reveal the surface-to-volume rate between *t*-ZrO₂ and *m*-ZrO₂, the BET measurement was undertaken. As summarized in Table 1, it can be concluded that, as the temperature increases and the crystal form changes, the surface area of the sample was decreased gradually. ZrO₂-400 possessed a relatively large BET surface area with 98.28 m²/g than other zirconium oxides. In fact, higher calcination temperature causes an obvious drop in the BET surface area and total volume, presumably due to particles crystallization. As comparison, the ZrO₂-500PA was prepared which has the surface area of 83.77 m²/g larger than that of *t*-ZrO₂.

Next, the *t*-ZrO₂ and *m*-ZrO₂ catalyst was further characterized by FT-IR, Pyridine-IR techniques. Fig. 3a exhibited the FT-IR spectra of the *t*-ZrO₂ and *m*-ZrO₂ catalysts. Therein, the broad peak at 3445 cm⁻¹ and several encountered peaks at the range of 1450 cm⁻¹ to 1800 cm⁻¹ could be attributed to the bending vibration of water on surface. This confirmed that ZrO₂ catalyst easily absorbed water. Moreover, the little peak at 741 cm⁻¹ and 598 cm⁻¹ are contributed to vibrations of the Zr–O group in the framework of zirconium oxide.

Pyridine infrared adsorption method is used to measure the surface acid type of these samples and the results are given in Fig. 3b. Therein, the adsorption at 1442 cm⁻¹ corresponds to the center of L acid, while the peak at 1594 cm⁻¹ is assigned to the hydrogen bonded pyridine on the catalyst surface [36]. Otherwise, the peak for the vibration of Brønsted acidity keeps very weak from the obtained IR spectra. Seen from the data (Fig. 3), it is found that there is no significant difference on the acid type of these two catalysts. Therefore, the catalytic performance is not closely related to the acid on the surface of the catalyst.

Furthermore, the difference in acidity strength and acid amount

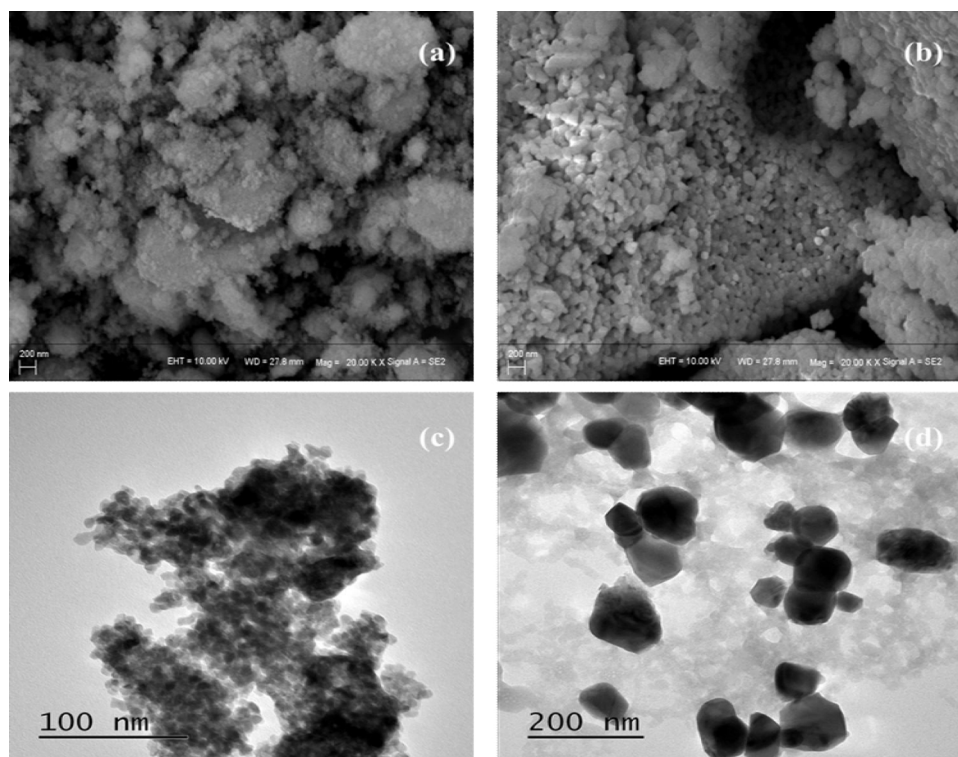


Fig. 2. SEM image of (a) *t*-ZrO₂, (b) SEM image of *m*-ZrO₂, (c) TEM image of *t*-ZrO₂, (d) TEM image of *m*-ZrO₂.

Table 1

The obtained physical properties of the prepared catalysts by BET detection.

Catalyst	BET Surface area (m ² g ⁻¹)	Pore Volume (cm ³ g ⁻¹)	Average pore diameter (Å)
ZrO ₂ -400	98.28	0.12	33.34
<i>t</i> -ZrO ₂	58.86	0.11	47.50
ZrO ₂ -700	19.88	0.11	103.03
<i>m</i> -ZrO ₂	11.32	0.06	71.94
ZrO ₂ -500PA ^a	83.77	0.15	42.69

^a The sample was prepared from Zr(OH)₄ with pore-making agent (melamine) by dehydration at 500 °C for 4 h in the air.

between *t*-ZrO₂ and *m*-ZrO₂ was also examined. Fig. 3c shows the results of NH₃-TPD experiment of both two catalysts, in which the weak to medium acidity occurs on the surface of *t*-ZrO₂ and the medium to strong acidity exists on the surface of *m*-ZrO₂ catalyst. However, the catalytic activity of *t*-ZrO₂ material is significantly higher than that of *m*-ZrO₂ catalyst. Thereby, the acidity strength and acid amount of *t*-ZrO₂ and *m*-ZrO₂ does not decide the difference of catalytic activity between the two kinds of catalysts which is different with that on homogeneous catalytic systems.

Fig. 3d presents the UV-vis spectra of *t*-ZrO₂ and *m*-ZrO₂. From the obtained spectra, it is found that absorption wavelength of *m*-ZrO₂ is larger than that of the *t*-ZrO₂. The shift of peak could be associated with the calcined temperature of precursor; along with the calcination temperature being increased, the particles of zirconia were aggregated, causing the ultraviolet absorption to move toward the long wavelength.

3.2. The reductive amination of cyclohexanone

The catalytic test on reductive amination of cyclohexanone is further carried out. Herein, the reductive amination of cyclohexanone was chosen as a model reaction at 140 °C for catalyst screening, where the *N,N*-dimethylformamide (DMF) was used as the solvent, amine source and reductant and the main product was *N,N*-dimethyl

cyclohexylamine (2) with the release of carbon dioxide (shown in the Scheme 2).

At first, the catalytic performances of different metal oxide were investigated and the data are provided in Table 2. It is found that a 44.3 % conversion of cyclohexanone with more than 99 % selectivity of 2 was obtained with *t*-ZrO₂ as the catalyst at 140 °C for 4 h under N₂ atmosphere (entry 1). Moreover, the conversion of 1 arrived at 72.6 % and product selectivity kept unchanged almost when a certain amount of water was added as promoter in the reductive amination (entry 2). Furthermore, when TiO₂, Al₂O₃ or CeO₂ was employed as catalyst, only 13.2 %, 7.7 % or 5.3 % conversion was achieved, respectively, though the selectivity of product could reach more than 99 % under the similar conditions (entries 3–5); these indicate that the common solid acid catalysts were not preferable to promote the reductive amination reaction. On the other hand, with the ZnO or MgO as catalyst, the conversion of 1 was less than 1 % or 6.4 % under same reaction conditions which shows that the basic metal oxides also not very useful to accelerate the transformation of cyclohexanone in the system (entries 6 and 7). For the *t*-ZrO₂ as comparison, reductive amination reaction was not occurred in the absence of any promotor, and less than 8.7 % conversion of 1 was obtained in the presence of single H₂O promotor (entries 8 and 9). These clearly revealed that *t*-ZrO₂ was an excellent catalyst for the reductive amination of cyclohexanone compared to the other metal oxides.

In order to further reveal the catalytic performance of zirconium oxide, the effect of different crystal structures of ZrO₂ was studied. Table 3 provides the results of reductive amination of cyclohexanone with the different ZrO₂ materials. Therein, the complete *t*-ZrO₂ or *m*-ZrO₂ crystals are produced when the zirconium oxide precursor was calcined at 500 °C or 900 °C during preparation. Meanwhile, the crystal structure of ZrO₂-600, ZrO₂-700, ZrO₂-800 was not complete and contains partial *t*- and *m*-type crystalline that have been verified by the above XRD patterns of these materials. The obtained experimental data showed that, due to the differences of crystals between *t*-ZrO₂ and *m*-ZrO₂, there exists a big gap of catalytic activity in reductive amination process (entries 1 and 5). In addition, for the ZrO₂-600, ZrO₂-700 and

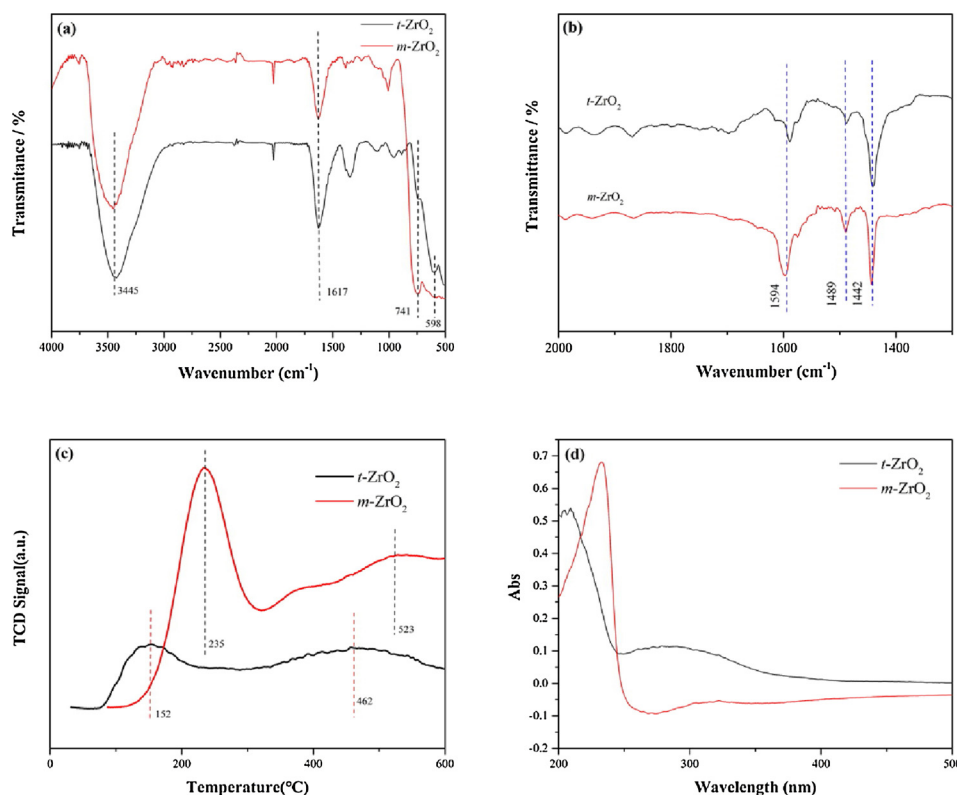
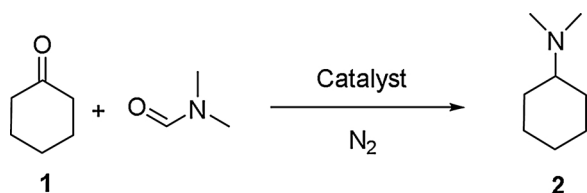


Fig. 3. (a) FT-IR spectra of *t*-ZrO₂ and *m*-ZrO₂; (b) Pyridine-IR spectra of *t*-ZrO₂ and *m*-ZrO₂; (c) NH₃-TPD results of *t*-ZrO₂ and *m*-ZrO₂ (d) UV-vis spectra of *t*-ZrO₂ and *m*-ZrO₂.



Scheme 2. The reductive amination of cyclohexanone.

Table 2
The reductive amination of cyclohexanone over different metal oxides^a.

Entry	Catalytic system	Promotor	Conversion of 1 (%) ^b	Selectivity of 2(%) ^b
1	<i>t</i> -ZrO ₂	–	44.3	> 99
2	<i>t</i> -ZrO ₂	H ₂ O	72.6	> 99
3	TiO ₂	H ₂ O	13.2	> 99
4	Al ₂ O ₃	H ₂ O	7.7	> 99
5	CeO ₂	H ₂ O	5.3	> 99
6	ZnO	H ₂ O	< 1	–
7	MgO	H ₂ O	6.4	> 99
8	–	–	< 1	–
9	–	H ₂ O	8.7	> 99

^a Reaction conditions: cyclohexanone (0.2 g), catalysts (0.05 g), H₂O (0.5 g) in DMF solvent (15 mL), at 140 °C, for 4 h, under 0.3Mpa of N₂.

^b The data are obtained by GC with the internal standard technique.

ZrO₂-800 catalyst, the conversion of 1 was gradually decreased along with the slow transition of crystal structure (entries 2–4). All these results exhibited that the catalytic activity of zirconium oxide on the reductive amination of cyclohexanone should be greatly influenced by the crystal structures of these materials. Herein, to study the effect of surface area, the ZrO₂-500PA was prepared whose surface area is higher than that of *t*-ZrO₂; while, the conversion of 1 with ZrO₂-500PA is lower than that using *t*-ZrO₂ as catalyst. Obviously, although the structures of

Table 3
Reactivity of zirconium oxide calcined at different temperatures^a.

Entry	Catalytic system	Promotor	Conversion of 1 (%) ^b	Selectivity of 2(%) ^b
1	<i>t</i> -ZrO ₂ (500)	H ₂ O	72.6	> 99
2	ZrO ₂ -600	H ₂ O	49.5	> 99
3	ZrO ₂ -700	H ₂ O	29.8	> 99
4	ZrO ₂ -800	H ₂ O	24.2	> 99
5	<i>m</i> -ZrO ₂ (900)	H ₂ O	4.0	> 99
6	ZrO ₂ -500 PA	H ₂ O	62.1	> 99
7 ^c	<i>t</i> -ZrO ₂	H ₂ O	100	> 99
8	ZrO ₂ -400	H ₂ O	71.8	> 99

^a Reaction conditions: cyclohexanone (0.2 g), zirconium oxide (0.05 g), H₂O (0.5 g) in DMF solvent (15 mL), at 140 °C, for 4 h, under 0.3Mpa of N₂.

^b The data are obtained by GC with the internal standard technique.

^c The reaction was performed at 160 °C.

both ZrO₂-500PA and ZrO₂-500 are tetragonal ones, the crystal purity of ZrO₂-500 catalyst should be higher than that of ZrO₂-500PA, which further verifies the significance of crystallinity on the selective transformation of 1 with zirconium oxide solid catalyst. Furthermore, it is found that a 100 % conversion of 1 with 99.0 % selectivity of 2 was attained when the reaction was performed at 160 °C. Otherwise, surface area of ZrO₂-400 catalyst is higher than that of *t*-ZrO₂; however, during the reductive amination processes, the conversion of 1 with ZrO₂-400 catalyst keeps a little lower than that obtained with *t*-ZrO₂, which reflected that Zr-OH species and surface area are not crucial for the reductive amination reaction.

To evaluate the stability of *t*-ZrO₂ material, the recycling experiment was also carried out. After first run, the used catalyst was collected *via* centrifugation and washed 3 times with ethanol. After being dried at 80 °C under vacuum and calcined at 500 °C, the *t*-ZrO₂ was recovered and rapidly added into the steel autoclave for the next run. Fig. 4 shows the experimental result and it is seen that the *t*-ZrO₂ still kept a high catalytic activity even after being reused for five cycles and

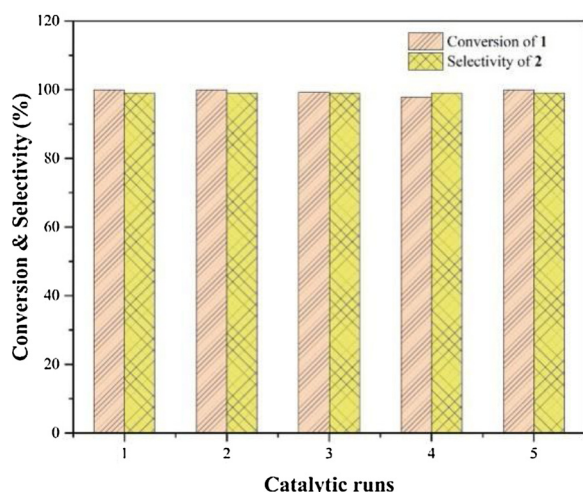


Fig. 4. The results for the recycling of $t\text{-ZrO}_2$ (Reaction conditions: 0.2 g of 1, 0.05 g $t\text{-ZrO}_2$, 0.5 g H_2O , 15 mL DMF, at 160 °C, under 0.3Mpa of N_2 , for 4 h).

both the conversion and selectivity of 2 arrived at > 99 % in the reductive amination of cyclohexanone with DMF. According to the data of BET detection and XRD pattern, the surface area of used catalyst was only decreased a little, and the crystal form of catalyst exhibited a slight change after reuse.

3.3. The study on the catalytic reaction mechanism

In order to reveal the catalytic reaction mechanism of reductive amination of 1 with $t\text{-ZrO}_2$ in DMF solvent, the control experiments and the corresponding theoretical calculation are performed, respectively. The experimental results were summarized in Table 4, it can be seen that the $t\text{-ZrO}_2 + \text{H}_2\text{O}$ should be responsible for the rapid decomposition of DMF (entries 1–3). The introduction of H_2O as the additive can mainly promote the formation of numerous hydroxyl group on $t\text{-ZrO}_2$ surface. Besides, the additions of pyridine and 2, 2'-dipyridine exhibited no substantial decrease of catalytic activities that the acid sites were not important on the reductive amination (Table 4, entries 7 and 8). These are consistent with results of the $\text{NH}_3\text{-TPD}$ studies.

Furthermore, the DFT calculation was also performed for the adsorption of DMF on the $m\text{-ZrO}_2(-1\ 1\ 1)$ and $t\text{-ZrO}_2(0\ 1\ 1)$ surfaces, which are main diffraction peaks based on obtained XRD pattern shown in Fig. 1. Herein, the adsorption of DMF at different sites of $m\text{-ZrO}_2(-1\ 1\ 1)$ and $t\text{-ZrO}_2(0\ 1\ 1)$ surface was calculated. The typical adsorbed configurations were shown in Fig. 5. It can be seen that the DMF molecule prefers to be adsorbed as the parallel configuration on the $t\text{-ZrO}_2(0\ 1\ 1)$ or $m\text{-ZrO}_2(-1\ 1\ 1)$ lattice plane (Figs. 5a and 5b). But the

adsorption energy for $t\text{-ZrO}_2(0\ 1\ 1)$ (-4.10 eV) is obviously larger than the one for $m\text{-ZrO}_2(-1\ 1\ 1)$ (-2.08 eV). On two crystal surfaces, the N and O atoms of DMF molecule coordinated to two Zr atoms. However, the N-Zr bond length is 2.22 Å for $t\text{-ZrO}_2(0\ 1\ 1)$ which is shorter than the N-Zr of 2.36 Å for $m\text{-ZrO}_2(-1\ 1\ 1)$.

The crystal structure of ZrO_2 also exhibited a significant effect on the N–C bond of DMF molecule. As shown in the Table S3 of supporting information, the bond energy in the gas phase is 498 kJ/mol, while the bond energy of the adsorbed molecule is decreased to 51 kJ/mol and 43 kJ/mol for $m\text{-ZrO}_2(-1\ 1\ 1)$ and $t\text{-ZrO}_2(0\ 1\ 1)$, respectively. Meanwhile, the length of C–N bond is stretched from 1.366 Å to 1.506 Å and 1.529 Å for $m\text{-ZrO}_2(-1\ 1\ 1)$ and $t\text{-ZrO}_2(0\ 1\ 1)$. The higher adsorption energy and the shorter Zr–N distance coupled with elongated C–N bond for $t\text{-ZrO}_2(0\ 1\ 1)$ indicated that DMF favorably adsorbs on tetragonal crystal than monoclinic crystal of ZrO_2 . This is consistent with our experimental results of higher conversion of cyclohexanone with $t\text{-ZrO}_2$ as the heterogeneous catalyst.

In the experimental investigations, it is concluded that the addition of water promoted the conversion of the reaction substrate. To identify the effect of water on the properties of ZrO_2 catalyst, the calculation for the adsorption of DMF on the hydroxylated ZrO_2 surface was carried out. As shown in Fig. 6, the adsorption configuration of DMF on the hydroxylated $t\text{-ZrO}_2$ surface was similar with that on pure $t\text{-ZrO}_2$ surface, in which the O and N atoms of DMF also bound with two Zr atoms on the surface. However, a hydrogen bond was formed between H atom of hydroxy and O atom of DMF on the hydroxylated $t\text{-ZrO}_2$ surface. Therefore, the DMF was furtherly pulled close to the catalyst surface with the decrease of O–Zr bond from 2.12 Å to 2.08 Å. The higher adsorption energy (-5.14 eV) for hydroxylated surface indicated that hydroxylated $t\text{-ZrO}_2(0\ 1\ 1)$ is substantially more active. This result is consistent with Salavati-fard's work, in which it is reported that hydrous ZrO_2 surface was more reactive than the dehydrated surface for Diels - Alder Cycloaddition using DFT method [37].

The density of state (DOS) profiles of dehydrated and hydroxylated surface were shown in Figs. 6c and 6d. It is clearly shown that the band gap is narrowed for the hydroxylated ZrO_2 surface, which was partially contributed to the hybridization of the p -band of O atom from DMF and the d -band of the Zr atom from the ZrO_2 surface at the site close to the Fermi level (as shown in Fig. 6e).

Furthermore, the Mulliken charge distribution (as shown in Table S4) revealed that 1.10 e and 1.14 e of electronic charge are transferred from ZrO_2 to the DMF, on the dehydrated and hydroxylated surface, respectively. It implied that there may be an electron donation and back-donation process occurring during the reaction. This means that the hydrous surface can promote the activity of ZrO_2 for the dissociation of the DMF molecule.

The catalytic reaction mechanism is proposed through the combination of experimental and simulation data. As shown in Scheme 3, the first step is that, with the assistance of H_2O , the adsorption of DMF on

Table 4
The results of control experiments^a.

Entry	Catalyst	Reaction System	Conv of 1 (%) ^b	Sele of 2 (%) ^b
1	$t\text{-ZrO}_2$	Compound 1 + anhydrous DMF + H_2O	96.6	> 99
2	$t\text{-ZrO}_2$	Compound 1 + anhydrous DMF	41.7	> 99
3	none	Compound 1 + anhydrous DMF + H_2O	11.3	> 99
4	none	Compound 1 + anhydrous DMF	7.9	> 99
5 ^c	none	Compound 1 + Dimethyl amine + Formic acid	92.9	> 99
6 ^c	none	Compound 1 + Dimethyl amine	15.8	0
7 ^d	$t\text{-ZrO}_2$	Compound 1 + anhydrous DMF + H_2O + Pyridine	66.6	> 99
8 ^e	$t\text{-ZrO}_2$	Compound 1 + anhydrous DMF + H_2O + 2, 2'-dipyridine	72.0	> 99

^a Reaction conditions: 0.2 g of 1, 0.05 g of catalyst, in 15 mL of anhydrous DMF, under 0.3 MPa of N_2 , reaction time 6 h, temperature 160 °C.

^b The data are obtained by GC with the internal standard technique.

^c The molar ratio of 1: dimethylamine: formic acid is 1: 5: 5 (33 wt% dimethylamine and 88 wt% formic acid aqueous solution), in a 15 mL of n-hexane solvent.

^d 0.2 g pyridine, temperature 140 °C.

^e 0.2 g 2, 2'-dipyridine, temperature 140 °C.

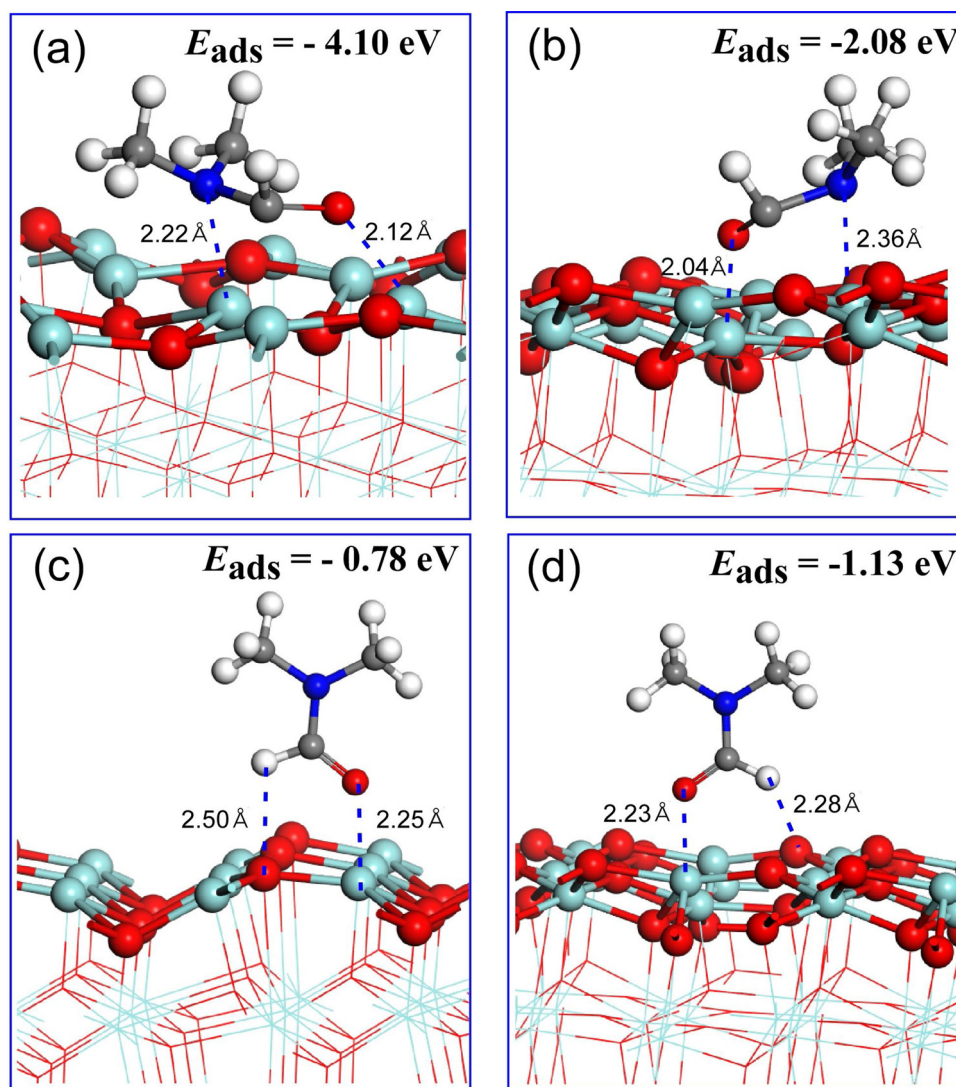


Fig. 5. The different adsorption structure of DMF on the *t*-ZrO₂(0 1 1) (a, c) and *m*-ZrO₂(-1 1 1) (b, d). The red ball is oxygen atom, the blue ball is nitrogen atom, the cyan ball is Zr atom, the grey ball is carbon atom, the white is hydrogen atom. The sublayer of ZrO₂ were shown as line model. (For interpretation of the references to colour in this figure legend, the reader is referred to the web version of this article).

the ZrO₂ surface. Then, the C–N bond of DMF is activated by the ZrO₂ + H₂O catalytic system, which has been proved by DFT simulation. Furthermore, the adsorbed DMF decomposes into the dimethyl amine and formic acid in a relatively low concentration (Figs. S7, S8 and S9). It has been confirmed by previous researches which refer that Zr(IV) tends to coordinate with the amide to form Zr(IV)-O and Zr(IV)-N that promotes decomposition of amide. Therefore, we inferred that dimethylamine attacks the carbonyl group, and formic acid loses a proton, leaving the oxygen on the carbonyl in the form of water, and the HCOO⁻ give own proton and turn itself into CO₂. In order to verify that the hydrogen in the methyl group of the product is originated from molecular DMF, we employed D₂O instead of H₂O, and the result showed that the methyl group of the product has no deuterated hydrogen, so the hydrogen in the product methyl group is all derived from DMF. So, we concluded that the departure of protons was sequential.

3.4. The selective reductive amination of different ketones and aliphatic aldehydes

Based on the above optimized reaction conditions, the selective transformation of other ketones and aliphatic aldehydes were also performed with the *t*-ZrO₂ catalyst. First, cyclohexanone derivatives,

cyclopentanone, cyclobutanone and branched-chain aldehydes as the substrates were examined in *N,N*-dimethylformamide solvent, and the corresponding data are presented in Table 5). Typically, the conversion of both 4-phenylcyclohexanone and 4-methylcyclohexanone arrived at 100 % (entries 1 and 2). As comparison, when 3-methylcyclohexanone was used as substrate, 87 % conversion and more than 99 % selectivity of *N,N*-3-trimethylcyclohexanamine was obtained where a relatively low conversion should be attributed to steric effect during the reaction (Table 5, entry 3).

Moreover, a 91 % conversion of cyclopentanone with > 99 % selectivity of *N,N*-dimethylcyclopentanamine was acquired, and 81.3 % conversion of cyclobutanone with > 99 % selectivity of was obtained under the similar conditions. These indicated that the angle of C–C bond in the ketone molecule is related to the reaction efficiency during the reductive amination processes (entries 4 and 5). Furthermore, it is found that, when several representative aliphatic aldehydes were used as the reactants, all the conversions of aldehydes were beyond 92.8 % at the 140 °C for 4 h (entries 6–9). Also, the reductive amination of other cycloalkanones and branched ketones were investigated and the results are presented in Table S2 of supporting information. It can be concluded that the steric hindrance of groups decreases the reaction efficiency, in which selectivities of corresponding products always keep

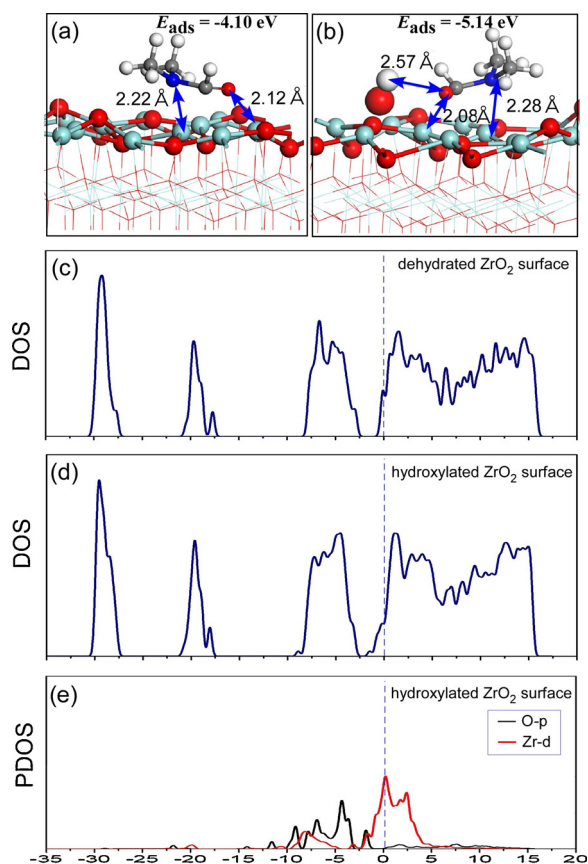
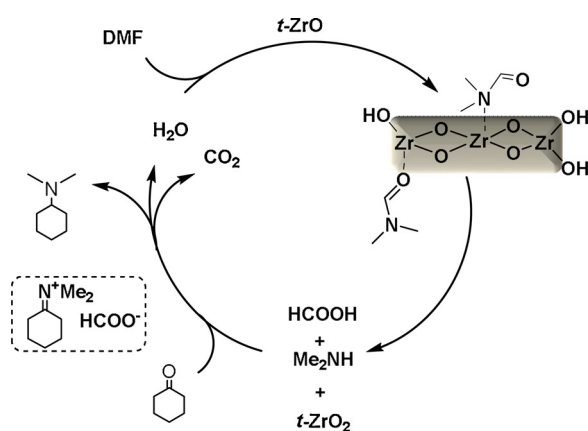


Fig. 6. (a) the adsorption structure of DMF on clean $t\text{-ZrO}_2(0\ 1\ 1)$, (b) the adsorption structure of DMF on hydroxylated $t\text{-ZrO}_2(0\ 1\ 1)$ surface, (c) total density of states (DOS) of the clean dehydrated $t\text{-ZrO}_2$, (d) DOS of the clean hydroxylated $t\text{-ZrO}_2$, (e) Partial DOS of p-band of O atom of adsorbed DMF and the d-band of surface Zr atom which interacted with O atom in the hydroxylated $t\text{-ZrO}_2$ system.



Scheme 3. Proposed reaction mechanism for reductive amination of cyclohexanone with $t\text{-ZrO}_2$ catalyst.

more than 99 % during all the reaction.

4. Conclusion

In summary, the reductive amination of ketones and aliphatic aldehydes to N,N -dimethyl derivatives are investigated with a simple $t\text{-ZrO}_2$ catalyst with DMF as both amine source as well as solvent. An excellent selectivity (> 99 %) of target product was obtained under the mild conditions. Therein, the reaction efficiency is closely related to the

Table 5

Reductive amination of different ketones and aliphatic aldehydes with $t\text{-ZrO}_2$ as the catalyst^a.

Entry	Substrates	Conversion (%) ^b	Selectivity of product (%) ^b
1		100	> 99 ^c
2		100	> 99 ^c
3		87.0	> 99
4		91.0	> 99
5		81.3	> 99
6 ^d		94.9	> 99
7 ^d		100	> 99
8 ^d		100	> 99
9 ^d		92.8	> 99

^a Reaction conditions: 0.2 g of reactant, 0.05 g of catalyst, in 15 mL of anhydrous DMF, under 0.3 MPa of N_2 , reaction time 6 h, temperature 160 °C.

^b The data are obtained by GC with the internal standard technique.

^c There exists conformational isomer.

^d The reaction is performed at 140 °C for 4 h.

steric effect during the reductive amination processes. Moreover, this excellent catalytic performance for $t\text{-ZrO}_2$ was related to higher adsorption energy (- 4.10 eV) and the shorter Zr-N distance (2.22 Å) than $m\text{-ZrO}_2$, and the DMF was further pulled close to the catalyst surface when addition of water. Furthermore, the $t\text{-ZrO}_2$ catalyst exhibited excellent stability that was reusable over multiple cycles without obvious loss of catalytic activity. Finally, based on the control experiments and simulation study, a possible reaction mechanism was proposed.

Declaration of Competing Interest

The authors declare no competing financial interest.

CRediT authorship contribution statement

Shun Wang: Writing - original draft, Data curation, Investigation. **Jiacong Li:** Writing - review & editing, Validation. **Ming Zhang:** Supervision. **Peng Bai:** Writing - review & editing. **Haigang Zhang:** Writing - review & editing, Investigation. **Xinli Tong:** Funding acquisition, Resources, Supervision, Validation, Writing - review & editing.

Declaration of Competing Interest

The authors report no declarations of interest.

Acknowledgement

This research work was financially supported by the General Program of the National Natural Science Foundation of China (No. 21878235), Tianjin Research Program of Application Foundation and Advanced Technology (No. 17JCYBJC20200) and the State Key Program of the National Natural Science Foundation of China (No. 21336008).

We also thank National Supercomputing Center in Shenzhen for providing the computational resources and materials studio 6.1.

Appendix A. Supplementary data

Supplementary material related to this article can be found, in the

online version, at doi:<https://doi.org/10.1016/j.mcat.2020.111108>.

References

- [1] J.R. Cabrero-Antonino, R. Adam, M. Beller, *Angew. Chem. Int. Ed.* 58 (2019) 12820–12838.
- [2] R.V. Jagadeesh, K. Murugesan, A.S. Alshammari, H. Neumann, M. Pohl, J. Radnik, M. Beller, *Science* 358 (2017) 326–332.
- [3] S.K. Sharma, J. Lynch, A.M. Sobolewska, P. Plucinski, R.J. Watson, J.M.J. Williams, *Catal. Sci. Technol.* 3 (2013) 85–88.
- [4] E. Pedrajas, I. Sorribes, K. Junge, M. Beller, R. Llusar, *Green Chem.* 19 (2017) 3764–3768.
- [5] J.S. Sapsford, D.J. Scott, N.J. Allcock, M.J. Fuchter, C.J. Tighe, A.E. Ashley, *Adv. Synth. Catal.* 360 (2018) 1066–1071.
- [6] B. Laroche, H. Ishitani, S. Kobayashi, *Adv. Synth. Catal.* 360 (2018) 4699–4704.
- [7] A.F. Abdel-Magid, S.J. Mehrman, *Org. Proc. Res. Dev.* 10 (2006) 971–1031.
- [8] G. Liang, A. Wang, L. Li, G. Xu, N. Yan, T. Zhang, *Angew. Chem. Int. Ed.* 56 (2017) 3050–3054.
- [9] T. Komanoya, T. Kinemura, Y. Kita, K. Kamata, M. Hara, *J. Am. Chem. Soc.* 139 (2017) 11493–11499.
- [10] H. Chen, L. Yan, H. Wei, *Organometallics* 37 (2018) 3698–3707.
- [11] F.I. McGonagle, D.S. MacMillan, J. Murray, H.F. Sneddon, C. Jamieson, A.J.B. Watson, *Green Chem.* 15 (2013) 1159–1165.
- [12] A.F. Abdel-Magid, K.G. Carson, B.D. Harris, C.A. Maryanoff, R.D. Shah, *J. Org. Chem.* 61 (1996) 3849–3862.
- [13] L. Legnani, B.N. Bhawal, B. Morandi, *Synthesis* 49 (2017) 776–789.
- [14] S. Bhattacharyya, *Synth. Commun.* 30 (2000) 2001–2008.
- [15] S. Nishimura, K. Mizuhori, K. Ebitani, *Res. Chem. Intermed.* 42 (2016) 19–30.
- [16] D. Chandra, Y. Inoue, M. Sasase, M. Kitano, A. Bhaumik, K. Kamata, H. Hosono, M. Hara, *Chem. Sci.* 9 (2018) 5949–5956.
- [17] D. Gülcemal, S. Gülcemal, C.M. Robertson, J. Xiao, *Organometallics* 34 (2015) 4394–4400.
- [18] H. Ghafuri, M.M. Hashemi, *Sci. Iran.* 19 (2012) 1591–1593.
- [19] Q.P.B. Nguyen, T.H. Kim, *Tetrahedron* 69 (2013) 4938–4943.
- [20] L. Yang, J. Lin, L. Kang, W. Zhou, D. Ma, *Adv. Synth. Catal.* 360 (2018) 485–490.
- [21] H. Zhang, X. Tong, Z. Liu, J. Wan, L. Yu, Z. Zhang, *Catal. Sci. Technol.* 8 (2018) 5396–5400.
- [22] J. Joo, T. Yu, Y.W. Kim, H.M. Park, F. Wu, J.Z. Zhang, T. Hyeon, *J. Am. Chem. Soc.* 125 (2003) 6553–6557.
- [23] Z. Liu, M.D. Amiridis, Y. Chen, *J. Phys. Chem. B.* 109 (2005) 1251–1255.
- [24] L. Liu, Y. Wang, C. Gao, C. Yang, K. Wang, H. Li, H. Gu, *J. Membrane Sci.* 592 (2019) 117368.
- [25] M. Eslamian, N. Ashgriz, *Powder Technol.* 167 (2006) 149–159.
- [26] M. Verma, V. Kumar, A. Katoch, *Mater. Chem. Phys.* 212 (2018) 268–273.
- [27] F.C.F. Marcos, J.M. Assaf, R. Giudici, E.M. Assaf, *Appl. Surf. Sci.* 496 (2019) 143671.
- [28] M. Fan, Z. Si, W. Sun, P. Zhang, *Fuel* 252 (2019) 254–261.
- [29] F.C.M. Woudenberg, W.F.C. Sager, J.E. Ten Elshof, H. Verweij, *J. Am. Ceram. Soc.* 87 (2004) 1430–1435.
- [30] J.P. Perdew, Y. Wang, *Phys. Rev. B* 45 (1992) 13244–13249.
- [31] J.P. Perdew, W. Yue, *Phys. Rev. B* 33 (1986) 8800–8802.
- [32] B.G. Pfommer, M. Côté, S.G. Louie, M.L. Cohen, *J. Comput. Phys.* 131 (1997) 233–240.
- [33] D.J. Chadi, *Phys. Rev. B* 16 (1977) 1746–1747.
- [34] M. Zhang, J. Zhuang, Y. Yu, *Appl. Surf. Sci.* 458 (2018) 1026–1034.
- [35] H.Y.T. Chen, S. Tosoni, G. Pacchioni, *Surf. Sci.* 652 (2016) 163–171.
- [36] E.P. Parry, *J. Catal.* 2 (1963) 371–379.
- [37] T. Salavati-fard, E.S. Vasiliadou, G.R. Jenness, R.F. Lobo, S. Caratzoulas, D.J. Doren, *ACS Catal.* 9 (2018) 701–715.